EPJ Web of Conferences **66**, 01017 (2014)
DOI: 10.1051/epjconf/ 20146601017
© Owned by the authors, published by EDP Sciences, 2014

From nuclear structure to neutron stars

Stefano Gandolfi[1] and Andrew W. Steiner[2]

[1] *Theoretical Division, Los Alamos National Laboratory Los Alamos, NM 87545, USA*
[2] *Institute for Nuclear Theory, University of Washington, Seattle, WA 98195*

Abstract. Recent progress in quantum Monte Carlo with modern nucleon-nucleon interactions have enabled the successful description of properties of light nuclei and neutron-rich matter. As a demonstration, we show that the agreement between theoretical calculations of the charge form factor of ^{12}C and the experimental data is excellent. Applying similar methods to isospin-asymmetric systems allows one to describe neutrons confined in an external potential and homogeneous neutron-rich matter. Of particular interest is the nuclear symmetry energy, the energy cost of creating an isospin asymmetry. Combining these advances with recent observations of neutron star masses and radii gives insight into the equation of state of neutron-rich matter near and above the saturation density. In particular, neutron star radius measurements constrain the derivative of the symmetry energy.

1 Introduction

In the last few decades, properties of nuclear systems have been successfully described by nucleon-nucleon potentials like Argonne and Urbana/Illinois forces, that reproduces two-body scattering and properties of light nuclei with very high precision [1, 2]. These nuclear potentials reproduce several properties of nuclear systems extremely well, including binding energies of ground- and excited states, radii, matrix elements, scattering states, and other observables [3–6].

The Argonne AV18 nucleon-nucleon interaction has small non-local terms and a hard core. Direct diagonalization of the Hamiltonian is not possible, and the expansion of the wave function on a finite basis, for example using no-core shell model or couple cluster methods, is computationally very expensive or unfeasible. In contrast, the use of correlated wave functions combined with Quantum Monte Carlo (QMC) methods has provided highly accurate solutions of the ground state of many-body nuclear systems [7].

The knowledge of the Equation of State (EoS) of pure neutron matter is an important bridge from the nucleon-nucleon interaction to neutron-rich matter. The symmetry energy $E_{\rm sym}$ is the difference of nuclear matter and neutron matter energy and gives the energy cost of the isospin-asymmetry in the homogeneous nucleonic matter. In the last few years the study of $E_{\rm sym}$ has received considerable attention (see for example Ref. [8] for a recent experimental/theoretical review). The role of the symmetry energy is essential to understand the mechanism of stability of very neutron-rich nuclei, and is also related to many phenomena occurring in neutron stars. The number of protons per baryon, x, is determined by beta-equilibrium and charge neutrality. These imply relationships between the chemical potentials and the symmetry energy, $\mu_e = \mu_n - \mu_p \approx 4E_{\rm sym}(1-2x)$. Matter near the nuclear

This is an Open Access article distributed under the terms of the Creative Commons Attribution License 2.0, which permits unrestricted use, distribution, and reproduction in any medium, provided the original work is properly cited.

Article available at http://www.epj-conferences.org or http://dx.doi.org/10.1051/epjconf/20146601017

saturation density is very neutron-rich, because electron degeneracy drives $\mu_n > \mu_p$. Thus neutron star matter is sensitive to $E_{\rm sym}$ and its first derivative. The inner crust of neutron stars, where the density is a fraction of nuclear densities, is mostly composed of neutrons surrounding a matter made of extremely-neutron rich nuclei that, depending on the density, may exhibit very different phases and properties. The extremely rich phase diagram of crustal matter is strongly related to the role of $E_{\rm sym}$. For example, it governs the phase-transition between the crust and the core [9] and the nature of r-mode instabilities [10, 11].

Neutron drops, neutrons confined by an external potential, provide a very simple model of neutron-rich nuclei, in which the core is modeled as an external potential acting on valence neutrons. In Refs. [12–14] neutron-rich oxygen isotopes were successfully described by neutrons confined in external wells, and in Ref. [15], the same model has been used to study calcium isotopes. More importantly, these systems describe inhomogeneous neutron matter that can be used as data for calibrating model energy density functionals in several conditions [16, 17]. The use of these functionals to study nuclei close to the neutron drip line requires then an important extrapolation to large isospin-asymmetries. This extrapolation is even more dramatic when the Skyrme forces are used to study the properties of the neutron star crust, where the matter is made by extremely neutron-rich nuclei surrounded by a sea of neutrons. For these reasons, *ab-initio* calculations of these systems starting from accurate nuclear Hamiltonians are important to constrain density functionals.

2 The Nuclear Hamiltonian and Quantum Monte Carlo

In our model, neutrons are non-relativistic point-like particles interacting via two- and three-body forces:

$$H = \sum_{i=1}^{A} \frac{p_i^2}{2m} + \sum_{i<j} v_{ij} + \sum_{i<j<k} v_{ijk}\,. \tag{1}$$

The two body-potential that we use is the Argonne AV8′ [18], that is a simplified form of the Argonne AV18 [1]. Although simpler to use in QMC calculations, AV8′ provides almost the same accuracy as AV18 in fitting NN scattering data [19]. The three-body force is not as well constrained as the NN interaction, but its inclusion in realistic nuclear Hamiltonians is important to correctly describe the binding energy of light nuclei [2].

The Urbana IX (UIX) three-body force has been originally proposed in combination with the Argonne AV18 and AV8′ [20]. Although it slightly underbinds the energy of light nuclei, it has been extensively used to study the equation of state of nuclear and neutron matter [21–23]. The Illinois forces have been introduced to improve the description of both ground- and excited-states of light nuclei, showing an excellent accuracy [2, 3], but it produces an unphysical overbinding in pure neutron systems [24, 25].

Another interesting class of nucleon-nucleon potentials are derived within the chiral effective field theory. Typically, these interactions have strong non-local terms, and as a consequence they cannot be easily included in QMC calculations. Recently it has been showed that these potentials can be designed to be local, and combined with QMC simulations [26]. However, the need to include a cutoff to the nucleon's momentum limits the applicability of chiral forces to study dense neutron matter. The cutoff of these potentials can be controlled in a many-body calculation [26], but the uncertainty is already quite large at saturation density in neutron matter, making the calculation at larger densities unfeasible.

We solve the many-body ground-state with a projection in imaginary-time, i.e.:

$$\Psi(\tau) = \exp[-(H - E_T)\tau]\Psi_v\,, \tag{2}$$

where Ψ_v is a variational ansatz, E_T is a normalization factor, and H is the Hamiltonian of the system. In the limit of $\tau \to \infty$, Ψ approaches the ground-state of H. The evolution in imaginary-time is performed by sampling configurations of the system using Monte Carlo techniques, and expectation values are evaluated over the sampled configurations. The main difference between GFMC and AFDMC is in the way that spin/isospin states are treated. In GFMC, all the spin/isospin states are explicitly included in the variational wave function. The results obtained are very accurate but limited to the ^{12}C [3] or 16 neutrons [16]. The AFDMC method samples the spin/isospin states using the Hubbard-Stratonovich transformation rather than sampling them explicitly [27]. The calculation can be then extended up to many neutrons, making the simulation of homogeneous matter and heavy nuclear systems possible [28]. The AFDMC has proven to be very accurate when compared to GFMC calculation of energies of neutrons confined in an external potential [16]. We shall present results obtained either using GFMC and AFDMC.

3 The Form Factor of ^{12}C

The spectra of light nuclei has been calculated using GFMC. Several ground- and excited-states are reproduced with high accuracy, with an average deviation with respect experimental measurements of the order of few keV for nuclei from deuteron up to ^{12}C. We have recently calculated also the form factor of ^{12}C and find excellent agreement with a compilation of experimental data [29].

The charge (and currents) operators are generally written by including one- and two-body operators:

$$\rho_q = \sum_i \rho_q(i) + \sum_{i<j} \rho_q(ij)\,. \tag{3}$$

The above operators are described for example in Ref. [30]

In Fig. 1 we show the GFMC results of the form factor. In this case the role of two-body operators is appreciable only for high momentum transfer $q \geq 3$ fm^{-1}. In all the range of momenta considered, the agreement between the calculation and experimental data is excellent. The same operators have been employed to calculate the electro-magnetic sum-rules of ^{12}C. Especially in the transverse sum-rule, the two-body operators (that are commonly neglected in similar calculations) contributes up to 50%. The large contribution given by the two-body currents has also been showed in early calculations of the Euclidean response in ^{4}He [31].

4 Neutron Drops

In the last few years, the energy and other properties of neutron drops have been studied by using ab-initio methods [16, 25] by confining neutrons in a harmonic oscillator (HO) or in a Wood-Saxon (WS) well. The QMC energy of neutron drops confined by V_{HO} is shown in Fig. 2 for two different frequencies of the external potential. The red points are the results obtained using the AFDMC method, and the blue ones using the GFMC. The two solid lines are the results given by using the original Skyrme SLy4 force [32], and a modified version. The energy is in units of the Thomas-Fermi energy, that is proportional to $\omega N^{4/3}$, to see the extrapolation to the thermodynamic limit. The two QMC methods agree within 1% for the $\hbar\omega = 10$ MeV trap, and the difference increases up to 4% for $\hbar\omega = 5$ MeV. The larger difference between GFMC and AFDMC for larger values of $\hbar\omega$ comes from the lack of pairing correlations in the AFDMC. At low densities neutrons are superfluids, and pairing correlations are quite important to include for open-shell configurations.

The difference between QMC and Skyrme at closed shells is mainly due to two effects, the bulk contribution and the gradient term. Skyrme forces typically give an EoS of pure neutron matter at

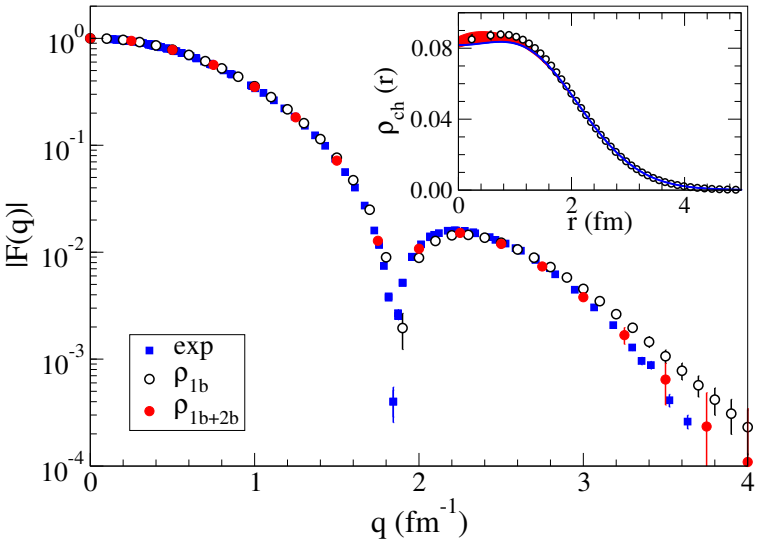

Figure 1. The form factor of ^{12}C calculated using GFMC with the AV18+IL7 Hamiltonian. The blue squares are experimental data, open black circles are the results obtained using only one-body charge operator and full red circles are the obtained with one- and two-body operators. In the inset we show the charge distribution in the nucleus, obtained with a Fourier transform of $F(q)$. The figure is taken from Ref. [29].

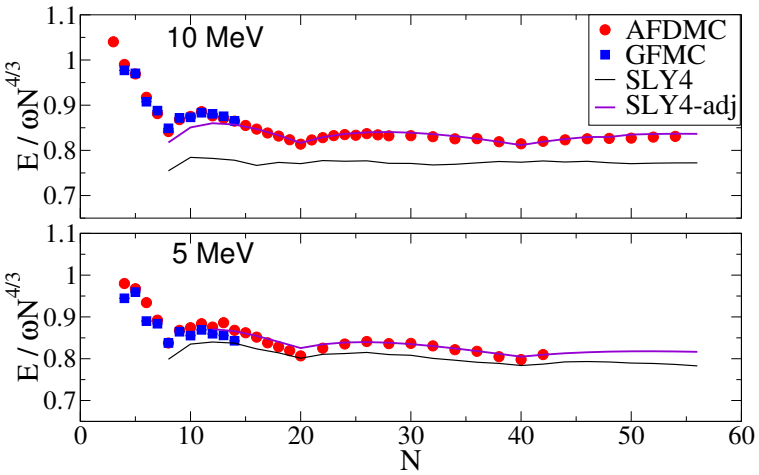

Figure 2. The energy of neutrons in a HO well with $\hbar\omega$ = 10 MeV (upper panel) and 5 MeV (lower panel) in units of $\omega N^{4/3}$. The red dots are the results given by AFDMC, blue squares are from GFMC, and the black line is the result obtained using the Skyrme SLy4. The violet line is the adjusted SLy4 where the strength of the gradient, pairing, and spin-orbit terms have been changed. The figure is taken from Ref. [16].

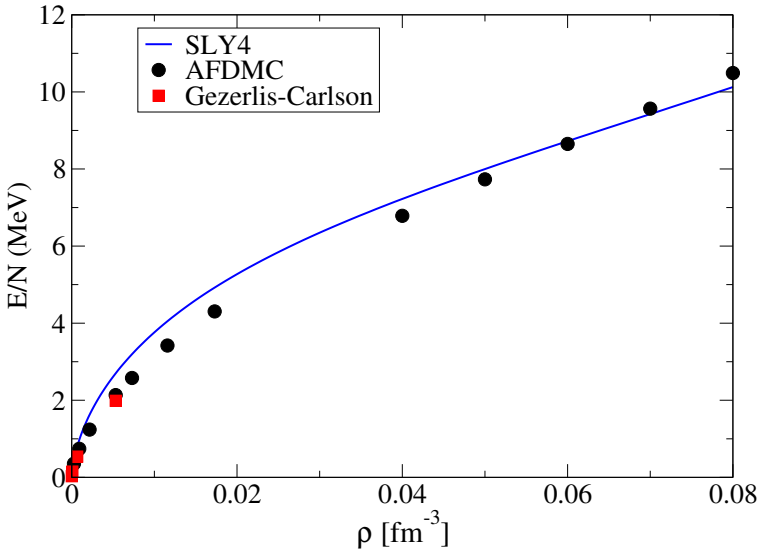

Figure 3. The equation of state of pure neutron matter. The AFDMC results [22, 33] are compared to the QMC results at low densities of Gezerlis and Carlson [34, 35], and to the equation of state of Skyrme SLy4 [36].

densities lower than saturation that is more repulsive than microscopic calculations. The equation of state of pure neutron matter is shown in Fig. 3 where we compare the AFDMC results from Refs. [22, 33, 37], the GFMC calculation of Gezerlis and Carlson [34, 35], and the equation of state given by SLy4. We make the reasonable assumption that Skyrme's bulk term cannot explain the difference between QMC and Skyrme energy in neutron drops. Then, since the pairing and the spin-orbit terms are expected to be very weak with respect to the gradient term for closed shell configurations, we can use the energy at N=8, 20 and 40 to re-adjust the gradient term of Skyrme. The energy of neutron drops with N near closed shells can be used to adjust the spin-orbit strength because for these configurations the pairing is not important. Finally, by comparing the energy of half-filled shells, we can tune the pairing term. In addition to the energy of neutrons in a HO potential, the adjusted SLy4 reproduces the energies in a WS well, radii and radial densities [16].

5 The Equation of State of Neutron Matter

In this section we present QMC results for pure neutron matter. There are several reasons to focus on pure neutron matter. First, the three-body interaction is non-zero only in the $T = 3/2$ isospin-channel (T is the total isospin of three-nucleons), while in the presence of protons there are also contributions in $T = 1/2$. The latter term is the dominant one in nuclei, and only weakly accessible by studying properties of nuclei. Second, the EoS of pure neutron matter is closely related to the structure of neutron stars.

We present several EoSs obtained using different models of three-neutron force in Fig. 4. The two solid lines correspond to the EoSs calculated using the NN potential alone and including the UIX three-body force [20]. The effect of using different models of three-neutron force is clear in the two bands, where the high density behavior is showed up to about $3\rho_0$. At such high density, the various

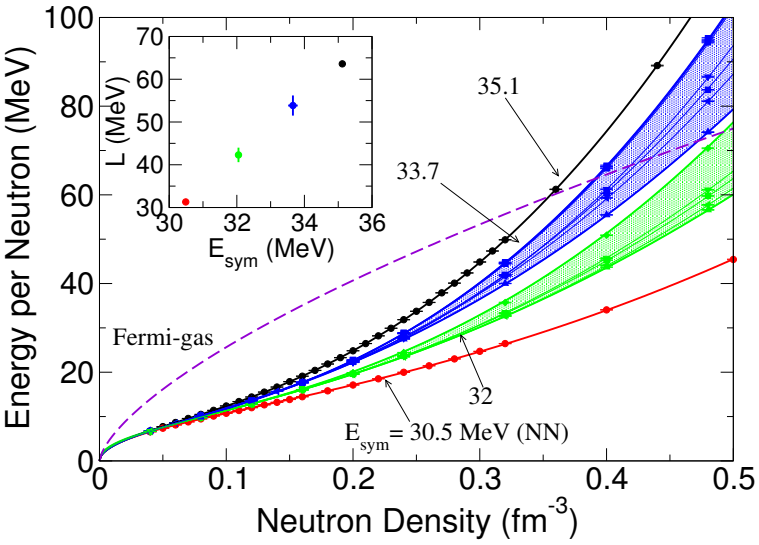

Figure 4. The QMC equation of state of neutron matter for various Hamiltonians. The red (lower) curve is obtained by including the NN (Argonne AV8′) alone in the calculation, and the black one is obtained by adding the Urbana IX three-body force. The green and blue bands correspond to EoSs giving the same $E_{\rm sym}$ (32 and 33.7 MeV respectively), and are obtained by using several models of three-neutron force. In the inset we show the value of L as a function of $E_{\rm sym}$ obtained by fitting the EoS. The figure is taken from Ref. [23].

models giving the same symmetry energy at saturation produce an uncertainty in the EoS of about 20 MeV. The EoS obtained using QMC can be conveniently fit using the following functional [22]:

$$E(\rho) = a\left(\frac{\rho}{\rho_0}\right)^{\alpha} + b\left(\frac{\rho}{\rho_0}\right)^{\beta}, \tag{4}$$

where E is the energy per neutron, $\rho_0 = 0.16$ fm^{-3}, and a, b, α and β are free parameters. The parametrization of the EoS obtained from different nuclear Hamiltonians is given in Ref. [23].

At ρ_0 symmetric nuclear matter saturates, and we can extract the value of $E_{\rm sym}$ and L directly from the pure neutron matter EoS. The result of fitting the pure neutron matter EoS is shown in the inset of Fig. 4. The error bars are obtained by taking the maximum and minimum value of L for a given $E_{\rm sym}$, and the curves obtained with NN and NN+UIX are thus without error bars. From the plot it is clear that within the models we consider, the correlation between L and $E_{\rm sym}$ is linear and quite strong.

6 Connection to Neutron Star Masses and Radii

Unlike the case of planets, which can have varying compositions for a fixed mass, the structure of neutron stars is determined mainly by the core, that is at first approximation compositionally invariant. Thus neutron star radii are determined principally by their mass, and to a good approximation all neutron stars lie on a universal mass-radius $M - R$ curve. When the EoS of the neutron star matter has been specified, the structure of an idealized spherically-symmetric neutron star model can be calculated by integrating the Tolman-Oppenheimer-Volkoff (TOV) equations.

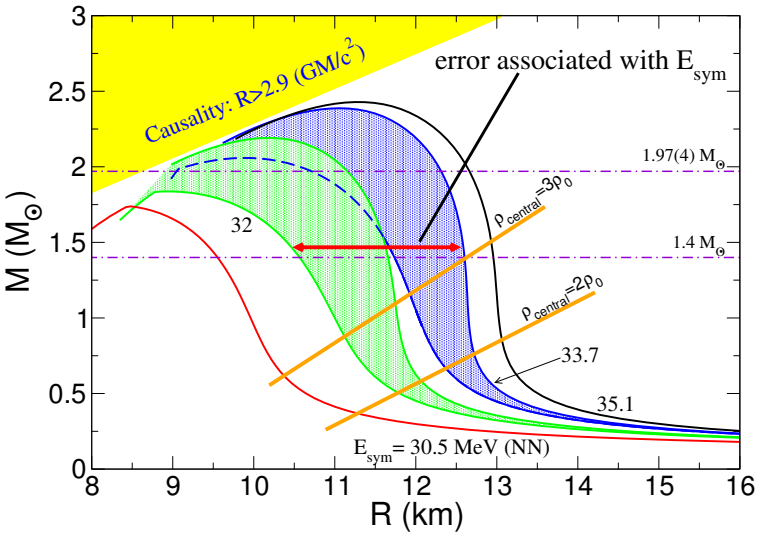

Figure 5. The mass-radius relation of neutron stars obtained from the EoS calculated using QMC. The various colors represent the $M - R$ result obtained from the corresponding EoSs described in Fig. 4. The two horizontal lines show the value of $M = 1.4$ and $1.97(4)M_\odot$ [38]. The figure is adapted from Ref. [23].

The neutron star mass measurements which provide the strongest EoS constraints are those which have the highest mass. Recent observations [38, 39] have found two neutron stars with masses near 2 $M_\odot$. These two data points provide some of the strongest constraints on the nature of zero-temperature QCD above the nuclear saturation density. We begin by examining what can be deduced about the M-R relation directly from these mass measurements, without employing a separate model for high-density matter. For lower densities we use the EoS of the crust obtained in Refs. [40] and [41]. For the core, we begin with the parametrization in Eq. 4, employing maximally stiff EoS when the QMC models violate the causality and become superluminal. The mass of a neutron star as a function of its radius is shown in Fig. 5. The two bands correspond to the result obtained using the two sets of EoS giving the same value of $E_{\rm sym}$ indicated in the figure. As in the case of the EoS, it is clear that the main source of uncertainty in the radius of a neutron star with $M = 1.4M_\odot$ is due to the uncertainty of $E_{\rm sym}$ rather than the model of the three-neutron force. The addition of a small proton fraction would change the radius R only slightly [21, 42], smaller than other uncertainties in the EoS that we have discussed. The numbers in the figure indicate the symmetry energy associated with the various equations of state. In the figure we also indicate with the orange lines the density of the neutron matter inside the star. Even at large masses the radius of the neutron star is mainly governed by the equation of state of neutron matter between 1 and 2 ρ_0 [43].

The AV8′ Hamiltonian alone does not support the recent observed neutron star with a mass of $1.97(4)M_\odot$ [38]. However, adding a three-body force to AV8′ can provide sufficient repulsion to be consistent with all of the constraints [23]. There is a clear correlation between neutron star radii and the symmetry energy which determines the EoS of neutron matter between 1 and 2 ρ_0. The results in Fig. 5 also show that the most modern neutron matter EoS imply a maximum neutron star radius not larger than about 13 km, unless a drastic repulsion sets in just above the saturation density. This tends

to rule out large values of L, typical of Walecka-type mean-field models without higher-order meson couplings which can decrease L.

7 Radius Measurements

In contrast to the mass measurements described above, neutron star radius measurements have proven more difficult, because they require both a distance measurement and some degree of modeling of the neutron star X-ray spectrum. Low-mass X-ray binaries (LMXBs) are neutron stars accreting matter from a low mass main-sequence or white dwarf companion. There are two types of LMXB observations which have recently provided neutron star radius information. The first type are LMXBs which exhibit photospheric radius expansion (PRE) X-ray bursts, thermonuclear explosions strong enough to temporarily lift the surface (photosphere) of the neutron star outwards [44, 45]. Several neutron stars have exhibited PRE X-ray bursts and four which have have been used to infer the neutron star mass and radius are given in the left panel of Fig. 6, using the methods described in Ref. [46]. The second type are quiescent LMXBs, (QLMXBs), where the accretion from the companion has stopped, allowing observation of the neutron star surface which has been heated by accretion [47]. A recent analysis of five neutron stars [48] including the possibility of both hydrogen and helium atmospheres and distance uncertainties is shown in the right panel of Fig. 6. Note that already from these two figures alone, it is clear that these probability distributions favor neutron star radii near 11 km. Although we will similar (R, M) distributions in our analysis below, it is important to remember that there are several systematic uncertainties which are potentially important. For the QLMXBs, the treatment of the X-ray absorption between the source and the observer, the flux calibration of the observing satellite, and the method used to measure the distance all play important roles. The situation for PRE X-ray bursts is even more challenging: complications such as spherical asymmetry, the time evolution of the spectra, and the location of the photosphere at "touchdown" may all modify the implied masses and radii.

8 Bayesian Analysis of Neutron Star Masses and Radii

In this section, we constrain the EoS and symmetry energy using observational data similar to that described in Sec. 7 and include the possibility of phase transitions in matter above the nuclear saturation density. In order to do this, we parametrize the EoS of matter at higher densities with a simple expression rich enough to include exotic matter. We perform a Bayesian analysis using data from QLMXBs and neutron stars which exhibit PRE bursts, where our model space is given by the EoS parameters and also one parameter for the mass of each neutron star in the data set. Given an EoS, the TOV equations provide the M-R curve and thus a prediction for the radius of each neutron star from its mass. As described above, we always ensure that our EoS are causal, hydrodynamically stable, and that our M-R curves support a 2 $M_\odot$ neutron stars.

It is important to note that these results are sensitive to several model assumptions and also sensitive to the EoS parametrization that we use. This is demonstrated in Table 1, where the 68% and 95% confidence limits are given for several different EoS parametrizations (top portion of the table) and variations in the interpretation of the data (bottom portion). The full specification of the models and data modifications is given in Ref. [49]. The first row (model A) is a baseline model where the high-density part of the EoS was described with two polytropes. The alternate EoS parametrization which most strongly changes the radius is that of model C, which treats the EoS as a set of line segments in the pressure-energy density plane. This allows for very strong phase transitions, typical of that obtained in a Maxwell construction where the pressure is very flat as a function of density.

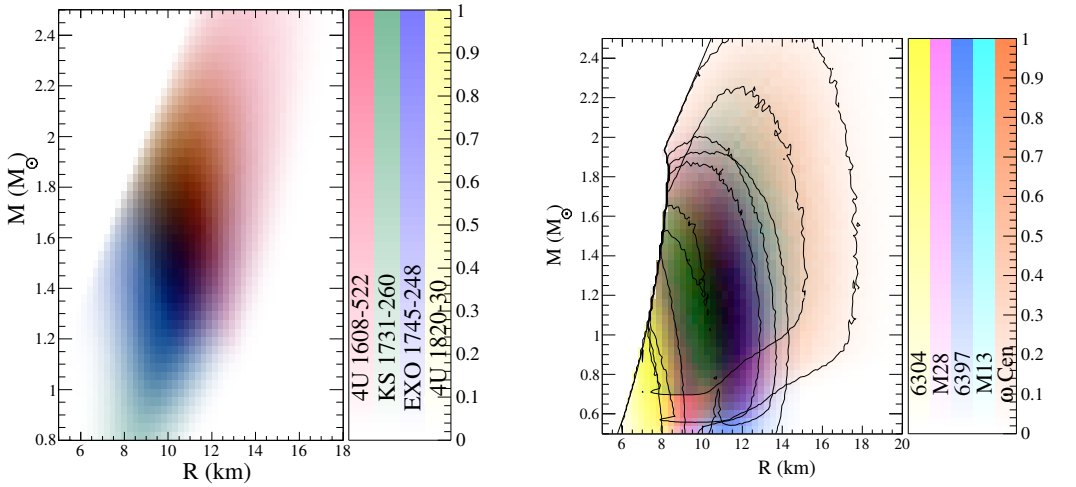

Figure 6. Left panel: Probability distributions in the mass-radius plane for four neutron stars exhibiting PRE X-ray bursts. Colors are added together in RGB color space. Right panel: Probability distributions in the mass-radius plane for five neutron stars in five globular clusters from Ref. [48]. Colors are added together in RGB color space when necessary. The contour lines outline the 90% confidence regions.

Table 1. Limits for the radius of a 1.4 solar mass neutron star for several different EoS models and interpretations of the data.

EoS model	Data modifications	$R_{95\%>}$ (km)	$R_{68\%>}$ (km)	$R_{68\%<}$ (km)	$R_{95\%<}$ (km)
	Variations in the EoS model				
A (2 polytropes)		11.18	11.49	12.07	12.33
B (2 polytropes)		11.23	11.53	12.17	12.45
C (line segments)		10.63	10.88	11.45	11.83
D (w/quarks)		11.44	11.69	12.27	12.54
	Variations in the data interpretation				
A	I (high f_C)	11.82	12.07	12.62	12.89
A	II (low f_C)	10.42	10.58	11.09	11.61
A	III ($z_{\rm ph} = z_{\rm NS}$)	10.74	10.93	11.46	11.72
A	IV (without X7)	10.87	11.19	11.81	12.13
A	V (without M13)	10.94	11.25	11.88	12.22
A	VI (no PREs)	11.23	11.56	12.23	12.49
A	VII (no qLMXBs)	11.17	11.96	12.47	12.81
Global limits		10.42	10.58	12.62	12.89

Model D describes a hybrid neutron star with deconfined quark matter at the core. In this case, the higher-density polytrope is replaced by the quark matter model of Ref. [50].

The largest uncertainty in the radius is obtained from the variation in f_C, the color correction factor. This factor describes the deviation of the X-ray spectrum from a black-body during the "cooling tail" of a PRE-burst. We also examine the variations in the radius after having removed extreme neutron

stars, or mass-radius distributions obtained from QLMXBs or PRE X-ray bursts. Over all of the changes we make to the EoS model and the interpretation of the data, the radius of a $1.4M_{\odot}$ neutron star lies between 10.4 and 12.9 km. Nevertheless, we have not tried all possible data interpretations and EoS models. Such a task is impossible, simply because there is no unambiguous way to enumerate a uncountably infinite parameter space (similar to the result that the cardinality of the real numbers is larger than that of the integers). Our choice of EOS models and data interpretations is thus necessarily biased, and this uncertainty is manifest as the prior distributions of our Bayesian analysis.

The final results for the $M-R$ curve and EoS are given in Fig. 7 from Ref. [49]. The $M-R$ curve obtained is relatively vertical, which naturally implies that almost all neutron stars have approximately the same radius. The EoS obtained from the mass and radius observations is also in concordance with results from quantum Monte Carlo and chiral effective theory described above and constraints obtained from heavy-ion collisions.

9 Determining the Density Dependence of the Symmetry Energy

In order to determine the symmetry energy, we use the parametrization of the neutron matter EoS from the quantum Monte Carlo results in Eq. 4 above. With this parametrization the symmetry energy at the saturation density $E_{\rm sym}$ and the parameter which describes the density dependence of the symmetry energy, L, are given by

$$E_{\rm sym} = a + b + 16\,, \quad L = 3\,(a\alpha + b\beta)\,. \tag{5}$$

Neutron stars contain a small amount of protons, so we multiply the EoS by a small ($\sim 10\%$) and density-dependent correction factor which modifies the pressure. This correction factor is obtained by averaging over Skyrme forces which give similar M-R curves to those suggested by the data. At some higher density $\rho_t \sim 0.24 - 0.48$ fm^{-3} the EoS may change due to the presence of exotic matter or a higher-order many-body correction. Beginning with this density, we employ a polytrope of the form $P = K_1\epsilon^{\Gamma}$, fixing K_1 to ensure that the EoS is continuous and setting $\Gamma_1 = 1 + 1/n_1$ where n_1 is the "polytropic index". At a higher energy density, ϵ_2, we use a second polytrope with index n_2, fixing K_2 to ensure that the EoS is continuous. This very similar to the "model A" described in Sec. 8 above. Generally, we find similar $M-R$ curves, independent of whether or not the neutron star contains quark matter in the core. We also find that the effect of varying ρ_t between 0.24 and 0.48 fm^{-3} is relatively small.

This analysis also provides posterior probability distributions for the EoS parameters. While we do not obtain significant constraints on a or α, the mass and radius data do constrain the parameters b and β (Fig. 8). While the simple parametrization employed in this section cannot fully describe the complexities of the nuclear three-body force, it does make it clear that astrophysical data is beginning to rule out some three-body forces which might otherwise be acceptable. We also show constraints on L. From neutron stars we obtain the constraints to the symmetry energy and slope to be $32 < E_{\rm sym} < 34$ MeV and $43 < \mathrm{L} < 52$ MeV within 68% confidence. The only way to obtain a larger value of L is through a strong phase transition just above the nuclear saturation density which tends to decouple the properties of matter at low- and high-densities. Thus model C from Sec. 8 above allows values of L as large as 83 MeV. However, it is not clear that such a strong phase transition at low densities is particularly realistic, as it might have been already ruled out by experimental work in heavy-ion collisions as reviewed in Ref. [8].

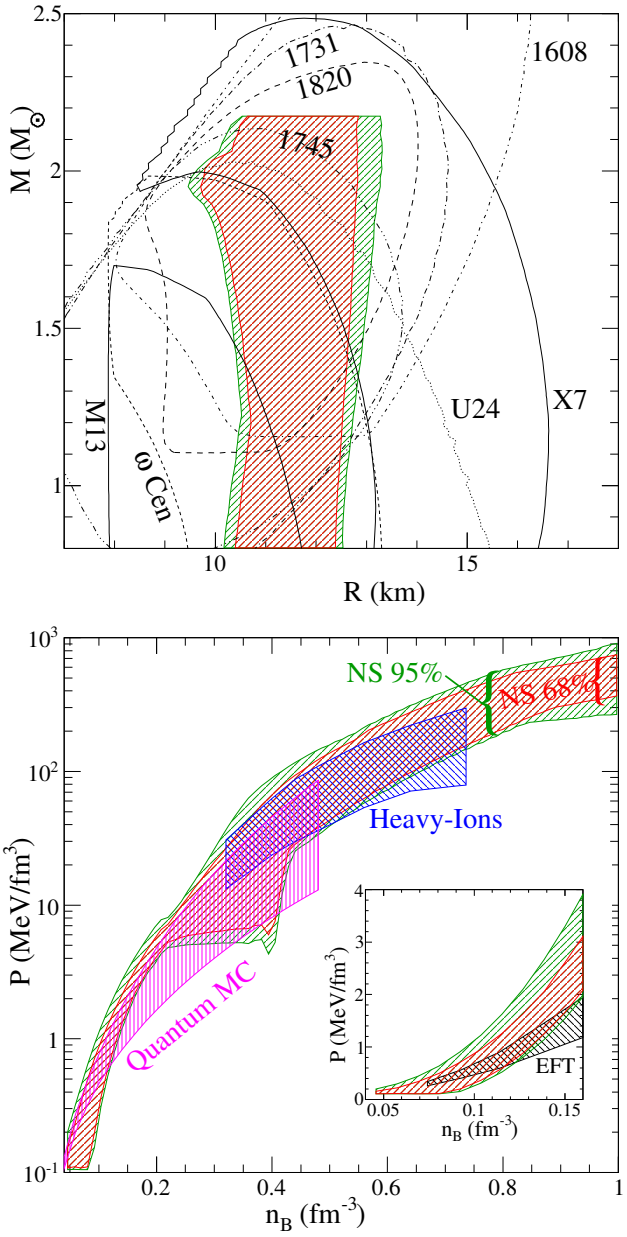

Figure 7. A comparison of the predicted *M*–*R* relation with the observations. The shaded regions outline the 68% and 95% confidences for the *M*–*R* relation; these include variations in the EoS model and the modifications to the data set (see Table 1) but not the more extreme scenarios. The lines give the 95% confidence regions for the eight neutron stars in our data set. The predicted pressure as a function of baryon density of neutron-star matter as obtained from astrophysical observations. The region labeled "NS 68%" gives the 68% confidence limits and the region labeled "NS 95 %" gives the 95% confidence limits. Results for neutron-star matter from effective field theory [51] (see inset), from quantum Monte Carlo [23], and from constraints inferred from heavy-ion collisions [52] are also shown for comparison.

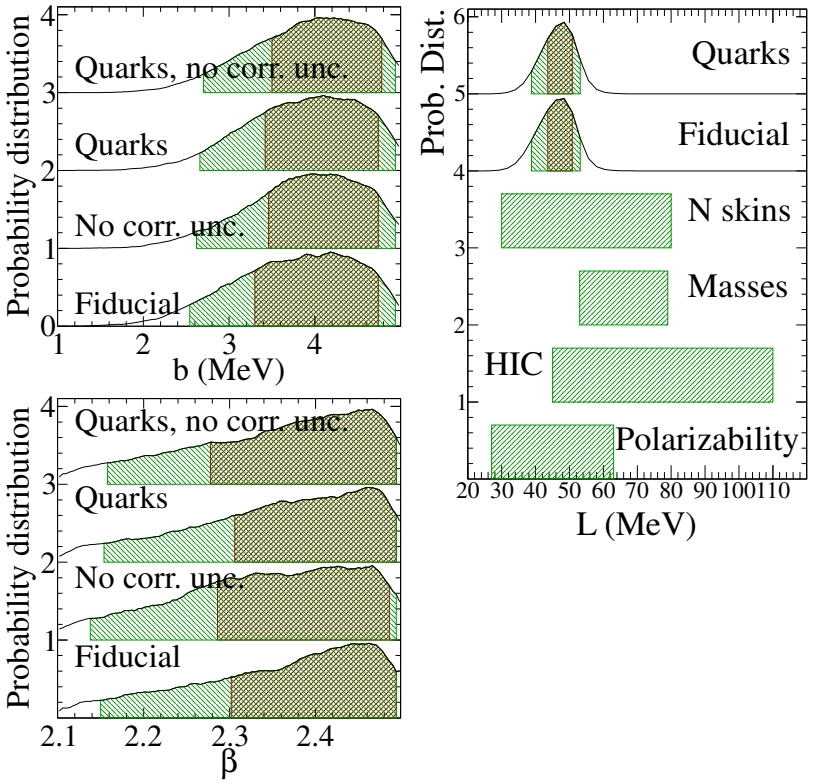

Figure 8. The left panel shows probability distributions of the parameters b and β obtained from the Bayesian analysis. The right panel summarizes constraints on L from observations and experiments. The top two curves show constraints on L as probability distributions assuming either the fiducial model of Ref. [53] or the model containing quarks. The bottom four curves show constraints on L from experiment, from neutron skins [54], nuclear masses [55], heavy-ion collisions [56], and from the electric dipole polarizability [57].

10 Acknowledgements

SG is supported by the U.S. Department of Energy, Office of Nuclear Physics, by the NUCLEI SciDAC program and by the LANL LDRD program. AWS is supported by DOE Grant No. DE-FG02-00ER41132.

References

[1] R.B. Wiringa, V.G.J. Stoks, R. Schiavilla, Phys. Rev. C **51**, 38 (1995)
[2] S.C. Pieper, V.R. Pandharipande, R.B. Wiringa, J. Carlson, Phys. Rev. C **64**, 014001 (2001)
[3] S.C. Pieper, AIP Conf. Proc. **1011**, 143 (2008)
[4] S.C. Pieper, R.B. Wiringa, Annu. Rev. Nucl. Part. Sci. **51**, 53 (2001)
[5] K.M. Nollett, S.C. Pieper, R.B. Wiringa, J. Carlson, G.M. Hale, Phys. Rev. Lett. **99**, 022502 (2007)

[6] R. Schiavilla, R.B. Wiringa, S.C. Pieper, J. Carlson, Phys. Rev. Lett. **98**, 132501 (2007)
[7] B.S. Pudliner, V.R. Pandharipande, J. Carlson, S.C. Pieper, R.B. Wiringa, Phys. Rev. C **56**, 1720 (1997)
[8] M.B. Tsang, J.R. Stone, F. Camera, P. Danielewicz, S. Gandolfi, K. Hebeler, C.J. Horowitz, J. Lee, W.G. Lynch, Z. Kohley et al., Phys. Rev. C **86**, 015803 (2012)
[9] W.G. Newton, M. Gearheart, B.A. Li, ArXiv e-prints (2011), 1110.4043
[10] D.H. Wen, W.G. Newton, B.A. Li, Phys. Rev. C **85**, 025801 (2012)
[11] I. Vidaña, Phys. Rev. C **85**, 045808 (2012)
[12] S.Y. Chang, J. Morales, V.R. Pandharipande, D.G. Ravenhall, J. Carlson, S.C. Pieper, R.B. Wiringa, K.E. Schmidt, Nuclear Physics A **746**, 215 (2004)
[13] S.C. Pieper, Nuclear Physics A **751**, 516 (2005)
[14] S. Gandolfi, F. Pederiva, S. Fantoni, K.E. Schmidt, Phys. Rev. C **73**, 044304 (2006)
[15] S. Gandolfi, F. Pederiva, S. A Beccara, European Physical Journal A **35**, 207 (2008)
[16] S. Gandolfi, J. Carlson, S.C. Pieper, Phys. Rev. Lett. **106**, 012501 (2011)
[17] S. Bogner, R. Furnstahl, H. Hergert, M. Kortelainen, P. Maris, M. Stoitsov, J. Vary, Phys. Rev. C **84**, 044306 (2011)
[18] R.B. Wiringa, S.C. Pieper, Phys. Rev. Lett. **89**, 182501 (2002)
[19] S. Gandolfi, J. Carlson, S. Reddy, A.W. Steiner, R.B. Wiringa, arXiv:1307.5815 (2013)
[20] B.S. Pudliner, V.R. Pandharipande, J. Carlson, R.B. Wiringa, Phys. Rev. Lett. **74**, 4396 (1995)
[21] A. Akmal, V.R. Pandharipande, D.G. Ravenhall, Phys. Rev. C **58**, 1804 (1998)
[22] S. Gandolfi, A.Y. Illarionov, K.E. Schmidt, F. Pederiva, S. Fantoni, Phys. Rev. C **79**, 054005 (2009)
[23] S. Gandolfi, J. Carlson, S. Reddy, Phys. Rev. C **85**, 032801 (2012)
[24] A. Sarsa, S. Fantoni, K.E. Schmidt, F. Pederiva, Phys. Rev. C **68**, 024308 (2003)
[25] P. Maris, J.P. Vary, S. Gandolfi, J. Carlson, S.C. Pieper, Phys. Rev. C **87**, 054318 (2013)
[26] A. Gezerlis, I. Tews, E. Epelbaum, S. Gandolfi, K. Hebeler, A. Nogga, A. Schwenk, Phys. Rev. Lett. **111**, 032501 (2013)
[27] K.E. Schmidt, S. Fantoni, Phys. Lett. B **446**, 99 (1999)
[28] D. Lonardoni, S. Gandolfi, F. Pederiva, Phys. Rev. C **87**, 041303 (2013)
[29] A. Lovato, S. Gandolfi, R. Butler, J. Carlson, E. Lusk, S.C. Pieper, R. Schiavilla, arXiv:1305.6959 (2013)
[30] G. Shen, L.E. Marcucci, J. Carlson, S. Gandolfi, R. Schiavilla, Phys. Rev. C **86**, 035503 (2012)
[31] J. Carlson, J. Jourdan, R. Schiavilla, I. Sick, Phys. Rev. C **65**, 024002 (2002)
[32] E. Chabanat, P. Bonche, P. Haensel, J. Meyer, R. Schaeffer, Phys. Scr. **T56**, 231 (1995)
[33] S. Gandolfi, A.Y. Illarionov, S. Fantoni, F. Pederiva, K.E. Schmidt, Phys. Rev. Lett. **101**, 132501 (2008)
[34] A. Gezerlis, J. Carlson, Phys. Rev. C **77**, 032801 (2008)
[35] A. Gezerlis, J. Carlson, Phys. Rev. C **81**, 025803 (2010)
[36] E. Chabanat, P. Bonche, P. Haensel, J. Meyer, R. Schaeffer, Nuclear Physics A **635**, 231 (1998)
[37] S. Gandolfi, A.Y. Illarionov, F. Pederiva, K.E. Schmidt, S. Fantoni, Phys. Rev. C **80**, 045802 (2009)
[38] P.B. Demorest, T. Pennucci, S.M. Ransom, M.S.E. Roberts, J.W.T. Hessels, Nature **467**, 1081 (2010)
[39] J. Antoniadis et al., Science **340**, 448 (2013)

[40] G. Baym, C. Pethick, P. Sutherland, Astrophys. J. **170**, 299 (1971)
[41] J.W. Negele, D. Vautherin, Nucl. Phys. A **207**, 298 (1973)
[42] S. Gandolfi, A.Y. Illarionov, S. Fantoni, J. Miller, F. Pederiva, K. Schmidt, Mon. Not. R. Astron. Soc. **404**, L35 (2010)
[43] J.M. Lattimer, M. Prakash, Astrophys. J. **550**, 426 (2001)
[44] J. van Paradijs, Astrophys. J. **234**, 609 (1979)
[45] F. Özel, G. Baym, T. Güver, Phys. Rev. D **82**, 101301 (2010)
[46] A.W. Steiner, J.M. Lattimer, E.F. Brown, Astrophys. J. **722**, 33 (2010)
[47] R. Rutledge, L. Bildsten, E. Brown, G. Pavlov, E. Zavlin, Astrophys. J. **514**, 945 (1999)
[48] J.M. Lattimer, A.W. Steiner, arXiv:1305.3242 (2013)
[49] A.W. Steiner, J.M. Lattimer, E.F. Brown, Astrophys.J. **765**, L5 (2013)
[50] M. Alford, M. Braby, M. Paris, S. Reddy, Astrophys. J. **629**, 969 (2005)
[51] K. Hebeler, A. Schwenk, Phys. Rev. C **82**, 014314 (2010)
[52] P. Danielewicz, R. Lacey, W.G. Lynch, Science **298**, 1592 (2002)
[53] A.W. Steiner, S. Gandolfi, Phys. Rev. Lett. **108**, 081102 (2012)
[54] M. Warda, X. Viñas, X. Roca-Maza, M. Centelles, Phys. Rev. C **80**, 024316 (2009)
[55] M. Liu, N. Wang, L. Z.-X., F.S. Zhang, Phys. Rev. C **82**, 064306 (2010)
[56] M.B. Tsang, Y. Zhang, P. Danielewicz, M. Famiano, Z. Li, W.G. Lynch, A.W. Steiner, Phys. Rev. Lett. **102**, 122701 (2009)
[57] A. Tamii, I. Poltoratska, P. von Neumann-Cosel, Y. Fujita, T. Adachi et al., Phys. Rev. Lett. **107**, 062502 (2011)